In Situ Analysis of Ultrashort Pulse Burst Ablation via Transmission Pump Probe Imaging

Benedikt Bornschlegel*[1], Martin Kratz[1], and Johannes Finger[2]

[1]*Chair for Laser Technology – RWTH Aachen University*
Steinbachstr. 15, 52074 Aachen, Germany
[2]*Fraunhofer Institute for Laser Technology ILT*
Steinbachstr. 15, 52074 Aachen, Germany
**Corresponding author's e-mail: benedikt.bornschlegel@llt.rwth-aachen.de*

Within the research topic of the application of high-power ultrashort pulsed (USP) laser beam sources to increase the productivity of USP processes different approaches are being pursued. Pulse bursts enable the utilization of higher average powers but shielding effects and heat accumulation are amplified by the small temporal and spatial distances between consecutive pulses. Additionally, the investigations on bursts have uncovered a new behavior for aluminum and copper, which is not fully understood yet. The article evaluates ex situ and in situ experiments for copper ablation with one to four pulses per burst. The varying ablation behavior between even and uneven numbers of pulses per burst are investigated and the changes in the ablation dynamics are described. The parameter variation for the ex situ experiments shows a dependency of the alternating efficiency effect on the applied pulse energy. Furthermore, the occurrence of this effect is demonstrated for single burst ablation on copper. Based on the comparison of the ex situ and in situ data obtained by pump probe transmission microscopy, the changing ablation dynamics for the different burst types are described qualitatively.

DOI: 10.2961/jlmn.2022.01.2004
Keywords: ultrashort pulsed, ablation, dynamic, in situ, pump probe, shock wave, copper

1. Introduction

Regardless of the superiority of ultrashort pulsed (USP) laser metal structuring with respect to precision and quality compared to longer pulsed laser ablation [1–3], USP processing is still only established in few industrial applications [4–6]. This circumstance is attributable to the relative low productivity achieved by conventional USP processes. Therefore, the application of new developed high-power ultrafast laser systems with average powers in the range of hundreds of Watt has been an important topic of the USP research for several years [4,7–12]. Since the optimum operating point for the most efficient ablation of metals is known to be in the range of e^2-times the ablation threshold [9,13] the application of high average powers is challenging. However, there are three promising approaches being investigated to overcome this limitation and bringing powers into effect: (1) The utilization of high repetition rates [4,12,14], (2) pulse bursts [6,15–18] and (3) the parallelization by multi-beam optics [11,19–22]. The multi-beam optic splits the laser beam in multiple partial beams and therefore the high pulse energy is distributed between these spots. The ablation processes are designed individually to find the optimal point for the most efficient ablation with manageable heat accumulation [23,24] of the residual heat within the multi-beam pattern [19,22]. The use of high repetition rates requires fast beam deflection to ensure a reasonable spot overlap as the influence of heat accumulation and shielding of the ablation products becomes stronger due to the small temporal separation [4,10]. However, the remaining process design strongly orientates towards conventional USP structuring. The application of pulse bursts is the only approach which does not require specific optics or deflection systems and can be implemented with conventional scanner and plane field optics. Therefore, it is the most universal approach and can be implemented on existing laser machining systems. It is based on replacing the single pulses of USP-processes with trains of pulses emitted with the laser seeder frequency, so called bursts. The commonly used seeder frequencies in the range of tens of megahertz lead to a small temporal separation compared to conventional USP processing. This results in a high influence of intra-burst heat accumulation and shielding effects. These effects significantly affect the achieved quality [25] and efficiency [18] of the burst processes. The increased temperature at the sample surface due to accumulation of residual heat of the individual laser pulses can reach the melting temperature of the material. This local melting can result in smoother surfaces. This effect is exploited for specific applications as tailored USP-polishing as surface finish [26]. Nevertheless, the precision of ablation processes is always affected by the surface melting. Absorption, scattering and reflection of laser radiation within ablation products are reducing the effective pulse energy at the material surface. Therefore, the process efficiency will drop. In addition to these effects, an alternating efficiency dependent on the number of pulses per burst has been reported for copper many times [6,16,18,27–30]. A hypothesis on material redeposition is postulated [27,30]. To get a deeper understanding of the shielding and redeposition, in situ pump probe microscopy in transmission mode is

applied for burst ablation of copper. Excitation, shielding and relaxation dynamics are investigated. The in situ transmission images of the ablation products of different burst modes are compared and matched with ex situ ablation experiments.

2. Experimental setups and procedures

For ultrashort pulsed laser ablation of cooper an alternating efficiency is reported which correlates with the number of pulses in a burst [6,16,18,27–30]. Processes with even numbers of pulses per burst (PpB) exhibit a lower efficiency than processes with uneven numbers of pulses per burst and single pulse ablation. For some setups even a more efficient ablation for 3 PpB compared with single pulsed ablation (1 PpB) is reported. The described effect decreases for higher number of pulses per burst. To exclude a dominating influence of the process conditions of scanner-based USP laser ablation ex situ multi- and single burst ablation experiments are carried out with a percussion drilling setup. A modified version of this setup is also used in the pump probe transmission microscopy.

2.1 Percussion drilling setup

For ex situ experiments on single- and multi-burst ablation in a percussion drilling setup a TruMicro2000 from TRUMPF is used. The circularly polarized laser radiation is focused with a lens with a focal length f = 75 mm resulting in a spot size of $2w_0 = 20$ µm diameter ($1/e^2$). The emitted central wavelength of the laser is $\lambda = 1030 \pm 3.7$ nm and the pulse duration can be tuned from $\tau = 500$ fs to 10 ps. For the following experiments the pulse duration is set to $\tau = 2$ ps. The system is capable of emitting pulse bursts with up to 8 PpB with a seeder frequency $f_{seed} = 50$ MHz. The maximum single pulse energy is reached at the basic repetition rate $f_{rep} = 400$ kHz. For the multi-burst experiments presented the repetition rate is set to 400 kHz. For the ex situ evaluation, the ablation depth is measured by white light interferometry. Scanning electron microscope (SEM) images are evaluated to resolve the single spot modification structures. For the ex situ experiments on copper (CW024A), bulk material samples and for the in situ experiments metal sheets are chosen, respectively. All samples are wet sanded in multiple steps and polished to achieve a high-quality surface finish.

2.2 Pump-probe setup

The in situ analysis in this work is carried out with the same burst ablation setup as for percussion drilling. The pump laser system is complemented by a second TruMicro2000 as probe laser system with a central wavelength of $\lambda_{Probe} = 515 \pm 0.9$ nm and a pulse duration of $\tau_{Probe} = 300$ fs. Both laser systems are based on the same seeder to provide a synchronous emission of pump and probe pulses. Additionally, this setup allows to skip the delay between pump and probe pulse by integer multiples of the seeder period of 20 ns. The temporal resolution below 20 ns is provided by a delay line. The delayed probe pulse is collimated and aligned orthogonally to the polished sample surface to establish a transmission exposure of the ablation products (cf. Fig. 1). Therefore, the probe beam is projected with a microscope lens through a bandpass filter on a CCD-camera. A high spatial and temporal resolution of 300 fs is provided by this setup.

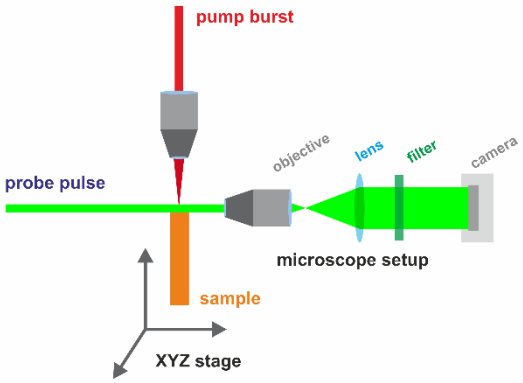

Fig. 1 Transmission pump probe microscopy setup for visualization of ablation products.

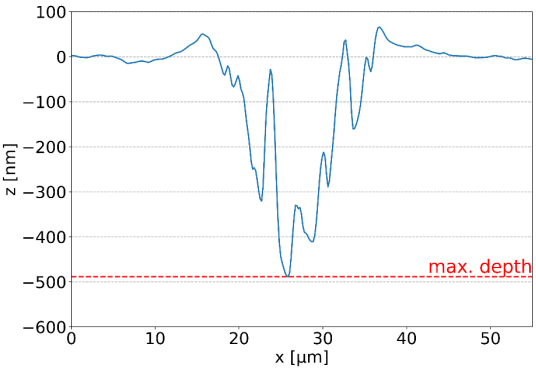

Fig. 2 Exemplary cross section through the crater center point taken of a white light interferogram for depth evaluation. The dashed line indicates the evaluation point of the highest depth reached. For each parameter set five identical processes are evaluated and averaged. (Single burst with 4 PpB, $\tau = 2$ ps, $f_{seed} = 50$ MHz, $F_0 = 5.0$ J/cm², $2w_0 \sim 20$ µm)

3. Experimental results

In the following, the ex situ results - measurement takes place after process completion - of multi- and single-burst ablation of copper are presented and discussed. Furthermore, the ex situ and in situ experiments for single burst ablation are compared. In the following, the term fluence always refers to the single pulse peak fluence $F_0 = \frac{2E_p}{\pi w_0^2}$ with the single pulse energy E_p and the beam radius w_0.

3.1 Ex situ results

For the ex situ experiments, the described percussion drilling setup is used to ablate copper with single- and multi-bursts. In order to compare the results to conventional USP laser ablation, the corresponding single pulses are processed with the same setup. A repetition rate of 400 kHz is used for all processes with multiple pulses and bursts. To evaluate the achieved ablation depth of the ablated craters a white light interferometer is used. Each parameter set is repeated five times in order to enable a statistic evaluation. Due to the rough surface after ablation the maximum ablation depth is evaluated. It is obtained by a cross section through the center of the crater as shown in Fig. 2 for a single burst with four pulses. The evaluation method is based on the assumption

that the ablation depth corresponds to the ablation volume within certain limits. Thus, particle redeposition outside the crater area and debris at the crater rim are not taken into account. With respect to the expected small ablation depth, the copper sample surface is pre-polished to Ra ≤ 35 nm.

The evaluated maximum ablation depth is shown in Fig. 3. In Fig. 4 the ablation depth normalized to the 1 PpB ablation depth is plotted for a total of 24 pulses. 1 to 4 PpB and single pulse peak fluences of 1.5 to 5.0 J/cm² are applied. In accordance with the literature, the ablation depth increases with the applied fluence for all pulses per burst. For two pulses in a burst, the absolute ablation depth decreases compared to the single pulse process and recovers slightly for bursts of three pulses. Only for single pulse fluences of 4.0, 4.5 and 5.0 J/cm², which are in the range of the optimum single pulse ablation fluence for copper, an increased ablation depth for 2 PpB is observed (cf. Fig. 4). For four pulses per burst, a decrease in ablation depth is visible. In Fig. 4, it is clearly illustrated that almost no significant alternating behavior for 1.5 J/cm² is measurable. No reliable measurements are achieved for fluences below 1.5 J/cm². Except for this weakened behavior for the lowest fluence, fluences from 2.0 to 5.0 J/cm² show an increase in relative ablation depth with increasing fluence. The single pulse ablation depth is exceeded applying 3 PpB and fluences of 4.0 J/cm² and greater, as already shown in Fig. 3. For 2 PpB, the relative ablation depth for 2.0 – 5.0 J/cm² is in the range of 0.5 – 0.7, decreasing with the fluence. Therefore, for the fluences 4.0 – 5.0 J/cm² almost no ablation of the second pulse is assumed. The 4 PpB ablation depth suggests, with exception of the lowest fluence, a rise and subsequent weakening of the achieved ablation depth for fluences from 2.0 to 5.0 J/cm². Yet, the values are very close to each other within the limits of measurement accuracy. However, both the increase of the ablation depth for fluences in the optimum range and the weaking of the alternating effect for low fluences are indicators for a dependency of this shielding effect on the applied energy. Nevertheless, a 100 % pulse overlap is present for these experiments caused by the percussion drilling setup. Thus, a shielding effect and heat accumulation of the pulses or bursts that are applied with a repetition rate of 400 kHz cannot be entirely excluded.

Single burst experiments are carried out and compared with the corresponding single pulse processes with the same number of pulses applied. For example, the ablation depth of one burst with four pulses is normalized to the ablation depth of four single pulses with repetition rate of 400 kHz. Due to the small ablation depth and the large surface roughness of the ablation craters, only the results of 5.0 J/cm² with reasonable ablation depths of 170 nm – 450 nm are shown in Fig. 5. For 2 PpB, the relative ablation depth drops to ~ 0.75 and reaches ~ 1.15 for 3 PpB but has no significant drop for 4 PpB. The missing drop of the relative ablation depth for 4 PpB could occur due to the rough melt structures within the crater which can result in locally greater depths (cf. Fig. 6). Therefore, the reduced ablation depth for 2 PpB is a burst-specific phenomenon that may be influenced by the conditions of a scanning structuring process but is already present in single burst ablation.

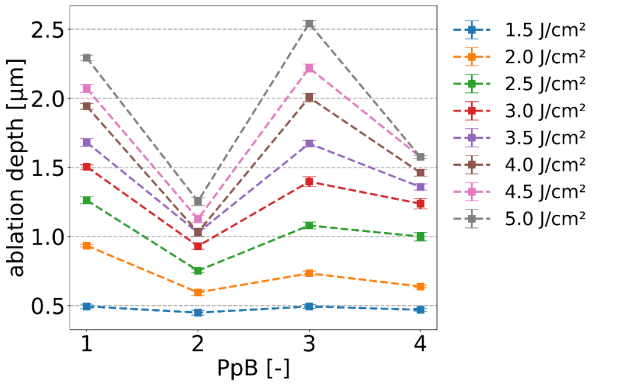

Fig. 3 Maximum ablation depth for 24 pulses in a percussion drilling process on copper with 1 – 4 PpB. (τ = 2 ps, f_{rep} = 400 kHz, f_{seed} = 50 MHz, F_0 = 1.5 – 5.0 J/cm², $2w_0$ ~ 20 µm)

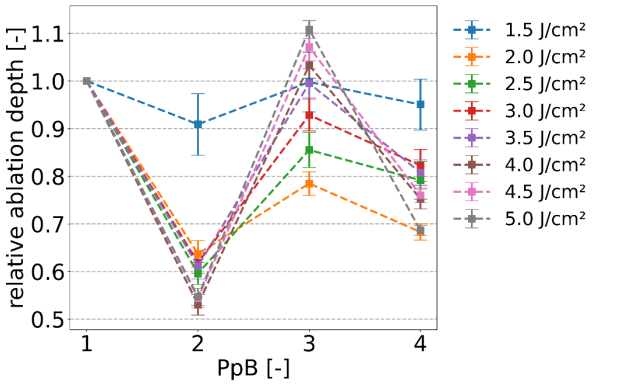

Fig. 4 Maximum ablation depth for 24 pulses in a percussion drilling process on copper with 1 – 4 PpB normalized to the single pulse ablation depth. (τ = 2 ps, f_{rep} = 400 kHz, f_{seed} = 50 MHz, F_0 = 1.5 – 5.0 J/cm², $2w_0$ ~ 20 µm)

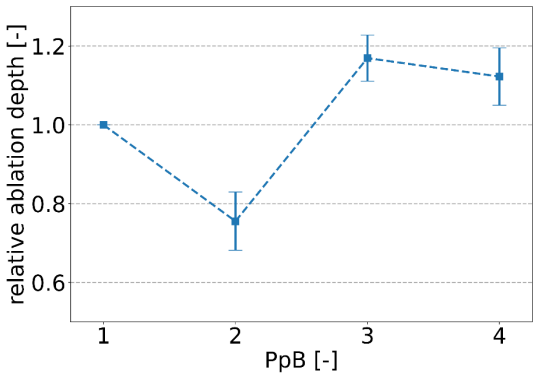

Fig. 5 Maximum ablation depth for single bursts on copper with 2, 3 and 4 PpB normalized to the single pulse percussion drilling process of 2, 3 and 4 pulses per shot. (τ = 2 ps, f_{rep} = 400 kHz, f_{seed} = 50 MHz, F_0 = 5.0 J/cm², $2w_0$ ~ 20 µm)

To investigate possible causes for the drop in ablation depth regarding burst ablation compared with single pulse processes, the remaining surface structures of the ablation craters are investigated by SEM. The SEM images of the craters are shown in Fig. 6. In the top row, three ablation craters for single pulse ablation with 2, 3 and 4 pulses applied are shown. The corresponding single burst ablation craters for 2, 3 and 4 PpB are illustrated in the bottom row. In all three cases thin random melt structures are generated by the single pulse ablation, which are very similar in

dimensions and appearance. In contrast to that, the three burst ablation craters differ significantly. For 2 PpB thicker melt structures close to the crater surface occur, which can be an indication for a disrupted ablation process. The process with 3 PpB shows melt structures slightly thicker than the corresponding single pulse process. The areas in between the resolidified melt structures are wider for the burst process. Furthermore, the pronounced secondary electron contrast for the 3 PpB structure indicates that the finest structures with the highest aspect ratio are present in this ablation crater compared to the other images. This effect indicates a fast resolidification of the material during an undisrupted and fast ablation process. The ablation crater for 4 PpB again shows thick melt structures even more pronounced and larger than in the 2 PpB burst process. This is a possible indication for an interrupted ablation of a molten material layer for 2 and 4 PpB which is then pushed back and resolidified on the surface. For 3 PpB, the solidification occurred during the detachment of the material and therefore the melt structure is oriented away from the surface.

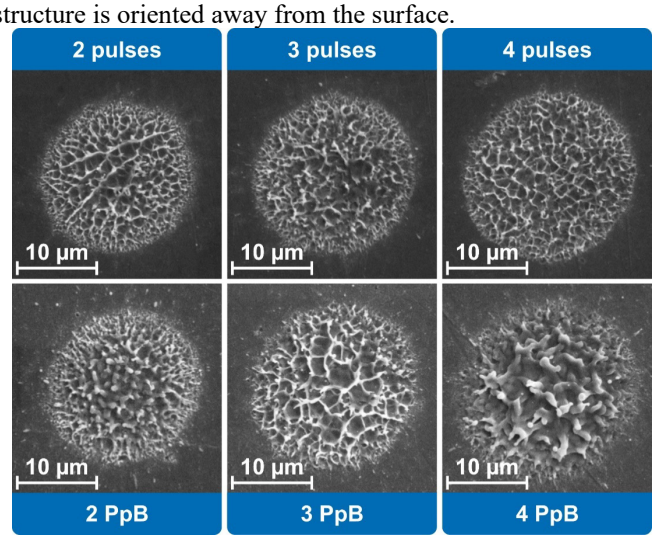

Fig. 6 Scanning electron microscope images of single burst ablation of copper with 2, 3 and 4 PpB (bottom row) and the corresponding percussion drilling process with single pulses (top row). (τ = 2 ps, f_{rep} = 400 kHz, f_{seed} = 50 MHz, F_0 = 5.0 J/cm², $2w_0$ ~ 20 µm)

3.2 In situ results

In order to investigate the ablation behavior of ultrashort pulse bursts on copper in situ, the transmission pump probe microscopy system described previously is used. A copper sheet with 0.5 mm thickness is used in order to reduce diffraction patterns at the edges of the sample. The surface of the sheet is polished to Ra < 50 nm to allow a reproduceable adjustment and a comparable surface finish. The ablation setup is adjusted as shown in Fig. 1 and the ablation spot center is positioned ~ 20 µm next to the edge of the sample to keep the full spot on the sample while simultaneously imaging the edge as sharp as possible. Images of the background (BG) as well as images of the ablation process (PI) are taken for every single process picture. The optical density (OD) is calculated with these measured intensity matrices using equation 1 to gain an optical density image for further evaluation (cf. Fig. 7).

$$OD_{xy} = \ln \frac{I_{BG_{xy}}}{I_{PI_{xy}}} \quad (1)$$

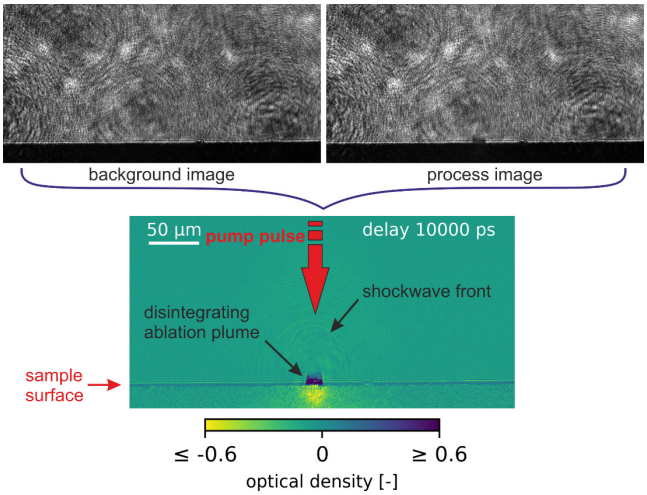

Fig. 7 Schematic sketch of the OD extraction from background and process image and indication of the observable image details.

On the one hand, negative values of the OD represent higher intensity compared to the background image for example caused by reflections of the probe beam at the microscope lens. On the other hand, positive values of the OD are interpreted as attenuations of the exposure beam due to ablation products or diffraction at the shock wave front.

In Fig. 8 - Fig. 11, the OD images of the ablation with 1 PpB with 50, 1000, 10000, 20050 and 40050 ps delay and for 2 - 4 PpB with 50, 1000, 2000, 5000 and 10000 ps delay after the last pulse of the burst are shown. Following, the ablation dynamics up to 10 ns after each burst are compared qualitatively. The bright spot (negative OD) at the sample front that is present in most of the images shown corresponds to the reflection of the microscope on the sample frontside lens illuminated by the process luminescence at the probe beam.

The single pulse ablation with 5.0 J/cm² is visualized in Fig. 8. Already after 50 ps, a strong attenuation at the sample surface is visible which indicates a dense ablation plume or a bulged molten material layer. For 400 – 500 ps delay, the first indications of shock wave generation occur which has already expanded to 15 µm height in the image for 1000 ps in Fig. 8**Fig. 1**. At about 4 - 5 ns delay the dense bulge above the surface grows in diameter (up to ~16 µm) and height (up to ~4 µm) when small parts start detaching from the bulge. As shown for 10 ns after the pulse, the bulge disintegrates into particles detaching from the surface until ~ 40 ns where the bulge is complete disintegrated. The particles ablated from the surface spread perpendicularly to the surface up to ~ 1 µs. For 1 µs to 10 µs only single particles still present in the surrounding atmosphere are imaged. The interpretation of a detaching and disintegrating molten material layer - called spallation [31–33]- would also be consistent with the observed melt structures for single pulse ablation within the craters (cf. Fig. 6) which are most likely formed by the formed cavities [32] below the sample surface.

In Fig. 9, the images of 50, 1000, 2000, 5000 and 10000 ps delay after the second pulse of a burst with two pulses are shown. From the moment of the arrival of the second pulse (20000 ps) the disintegrating ablation plume of the first pulse becomes denser again and the formation of a shock wave channel above the ablation products of the first pulse is visible, which is shown for 20050 ps in Fig. 9. The

channel formed has a similar diameter as the ablation plume (~ 18 µm) of the first pulse and is formed in the entire height of the shock wave front at that time (~ 72 µm). This observation indicates a partial absorption of the second pulse in the ablation plume and supports the shielding effect theory. The shock wave channel spreads symmetrically as an ellipsoid until ~ 22 ns when the bottom of the ellipsoid reaches the sample surface (cf. Fig. 9). This leads to a deformation of the ellipsoid into a paraboloid with a protrusion at the sample surface. At 24 -25 ns delay, the second shock wave catches up with the decelerated first shock wave front which is consequently deformed. The remains of the first ablation plume disappear. A reason for this could be the evaporation and spreading within the shock wave volume or more likely the redeposition by the part of the elliptic shock wave front that is directed downward. In both cases the ablation process of the first pulse is disturbed. There is no indication of particles detaching from the plume and the sample surface after the second pulse within this period of time. For 24 – 25 ns, a strong ablation plume becomes visible that disintegrates into particles until, at 100 -120 ns, the dense plume at the surface is completely disintegrated. Particles moving away from the surface are visible until 1.5 – 2 µs. Only single particles are imaged in the surrounding atmosphere until 10 µs like for the single pulse ablation. The presence of the dissolving ablation plume next to the surface for 2 PpB, which is 60 – 80 ns longer compared to the single pulse ablation could match as an indicator for more pronounced melt dynamics on the surface which corresponds to the SEM images in Fig. 6.

In Fig. 10, the ablation dynamic for three pulses per burst is shown during the first 10 ns. In contrast to 2 PpB, no visible shock wave channel is generated at the impact time of the third pulse and only an increase in density of the ablation plume can be observed. This again is an indication for the partial absorption of the laser pulse in the existing ablation plume. Following, the particles that started to detach from the ablation plume disappear until 41 ns and the ablation process of the second pulse is interrupted. At 41 – 42 ns a semitransparent hemisphere is formed above the dense ablation plume which spreads into the half-space (cf. Fig. 10 for 45000 ps and 50000 ps) until it reaches the shock wave front between 50 and 60 ns. Most likely this hemisphere consists of a vapor phase within an expanding shock wave front, indicating a non-negligible share of vapor-based ablation during the ablation process of the third pulse. Considering the distribution of the semitransparent phase within the hemisphere the preferred direction of propagation of this ablation products is lateral. This vapor phase could be one reason for the more efficient ablation with 3 PpB compared to 1 PpB. The semitransparent phase is observed up to 80 – 100 ns within the shock wave front. The disappearance of the semitransparent phase is most likely caused by dilution due to spreading in the growing shock wave. However, there is still a remaining dense ablation plume at the sample surface until it disintegrates completely into particles at 100 -120 ns which move away from the surface until 1.5 – 2 µs. As for the single and double pulse ablation until 10 µs, only single particles are imaged in the surrounding atmosphere. The shorter duration of the disintegration of the ablation plume into particles compared to 2 PpB indicates a less pronounced melt dynamic and a faster ablation process for 3 PpB, which is consistent with the ex situ observations.

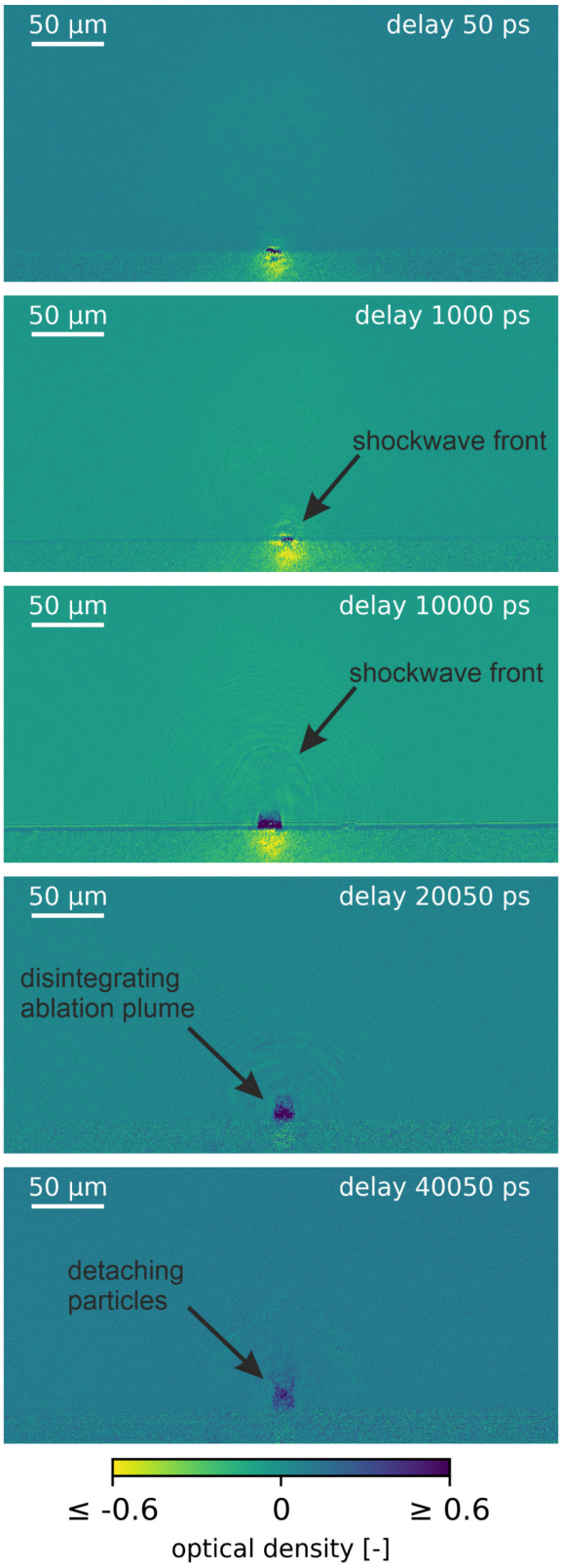

Fig. 8 Transmission pump probe images for 1 PpB with 50, 1000, 10000, 20050 and 40050 ps delay to the pulse. (τ = 2 ps, f_{rep} = 400 kHz, f_{seed} = 50 MHz, F_0 = 5.0 J/cm², $2w_0$ ~ 20 µm)

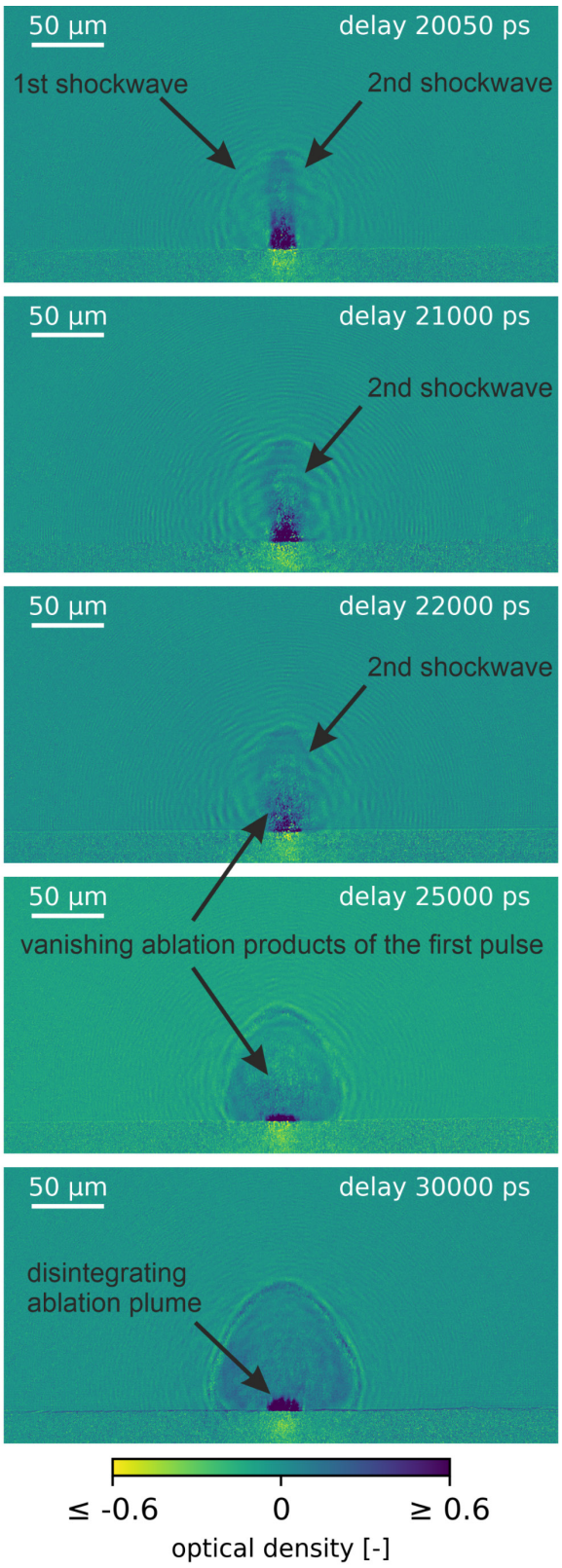

Fig. 9 Transmission pump probe images for 2 PpB with 20050, 21000, 22000, 25000 and 30000 ps delay to the first pulse. (τ = 2 ps, f_{rep} = 400 kHz, f_{seed} = 50 MHz, F_0 = 5.0 J/cm², $2w_0$ ~ 20 µm)

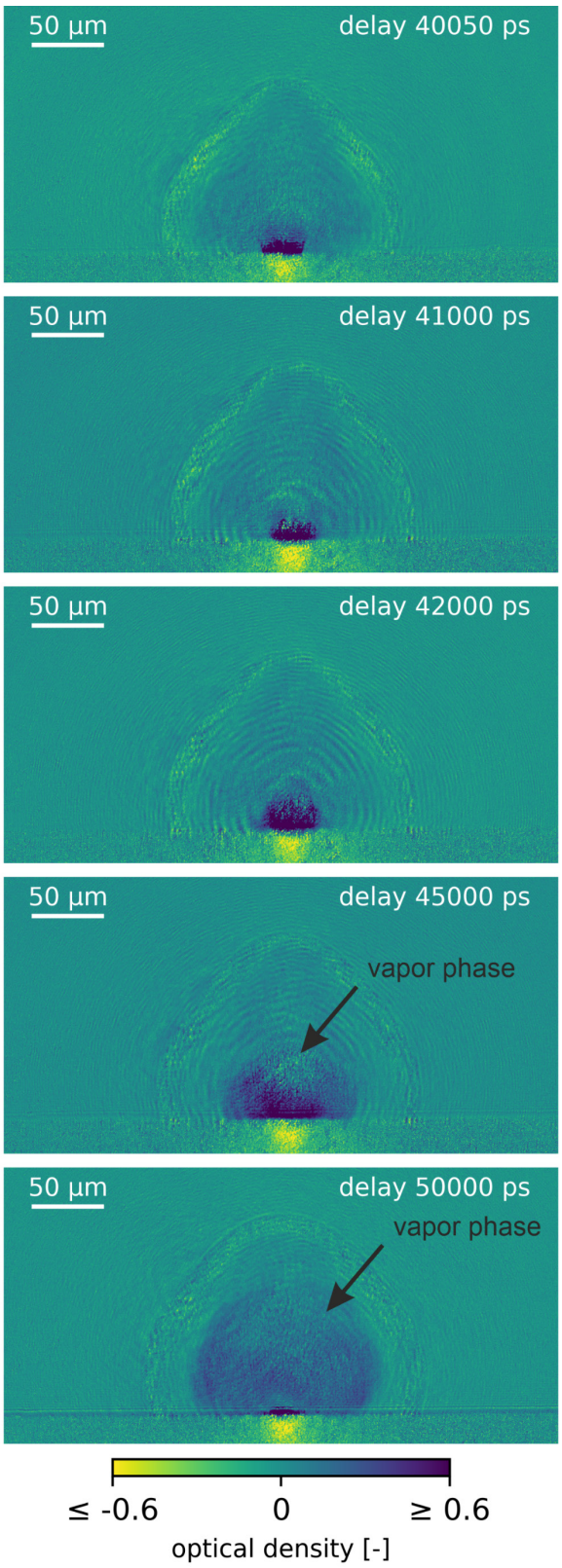

Fig. 10 Transmission pump probe images for 3 PpB with 40050, 41000, 42000, 45000 and 50000 ps delay to the first pulse. (τ = 2 ps, f_{rep} = 400 kHz, f_{seed} = 50 MHz, F_0 = 5.0 J/cm², $2w_0$ ~ 20 µm)

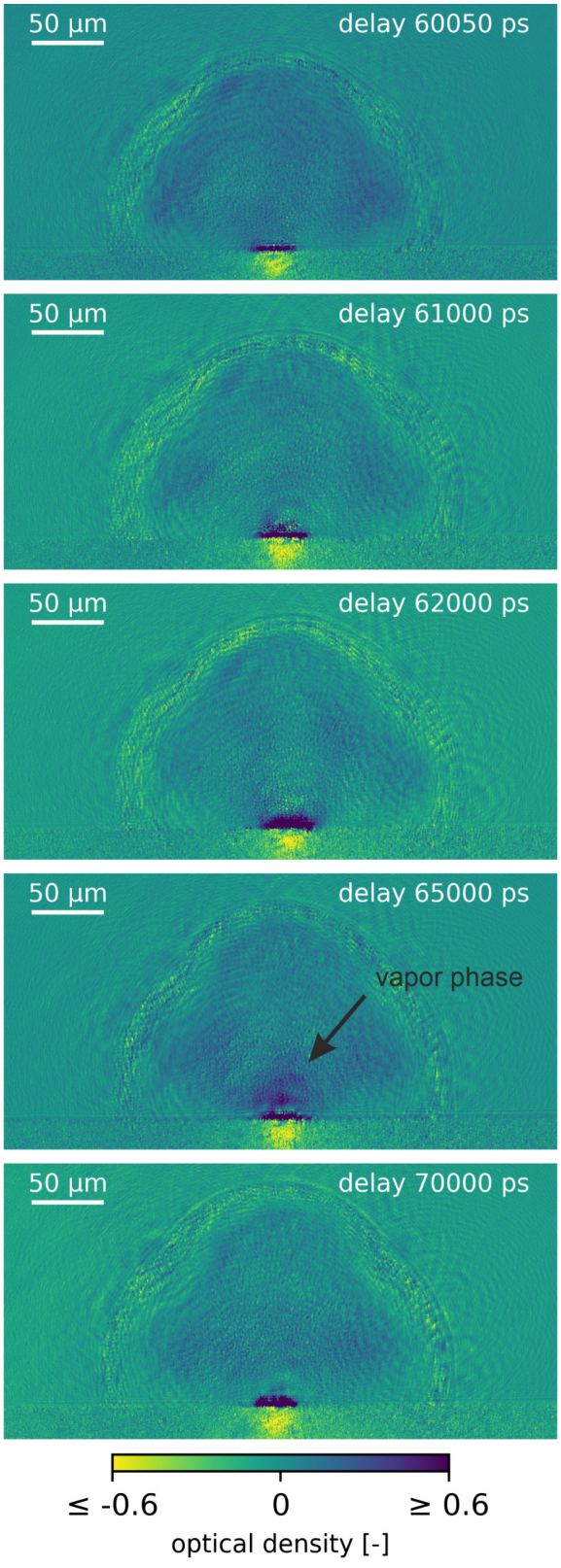

Fig. 11 Transmission pump probe images for 4 PpB with 60050, 61000, 62000, 65000 and 70000 ps delay to the first pulse. (τ = 2 ps, f_{rep} = 400 kHz, f_{seed} = 50 MHz, F_0 = 5.0 J/cm², $2w_0$ ~ 20 µm)

In Fig. 11, the ablation dynamic of the fourth pulse is depicted. In contrast to the second and third pulse no significant change in the ablation plume can be observed at the time of the pulse arrival, although the existing dense ablation plume at the surface is growing in height until 62 ns. From 62 to 68 ns a small patch of semitransparent ablation plume separates from the dense plume at the surface and spreads within the shock wave (cf. Fig. 11 65000 ps) which is similar to 3 PpB presumably due to a share of vapor-based ablation. For 70 to 80 ns particles start detaching from the dense ablation plume until it is fully disintegrated at ~ 120 – 140 ns. The directed ablation dynamic of the particles is observable until 2 – 2.5 µs and from this point until 10 µs only particles remaining in the atmosphere can be imaged.

4. Conclusion

The alternating efficiency for the USP burst ablation of copper that has already been reported several times is studied in this work. A purely process-based effect is excluded by ex situ multi- and single-burst ablation experiments. An influence of the conditions of a real machining process is likely and cannot be excluded here. Comparing the ex situ and in situ results presented in this work a change of the ablation dynamics for each burst type with the number of pulses applied becomes evident. For single pulses (1 PpB) an opaque bulge at the surface that disintegrates into particles is observed. The particles detach unhindered from the surface and move away in an ablation plume perpendicularly to the surface. The shock wave front propagates almost as hemisphere and is decelerated by the surrounding atmosphere. These observations combined with the information about the melt structures for single pulse ablation supports the assumption of a molten spallation layer which is separating from the surface. For 2 PpB the ablation process of the first pulse is most likely interrupted by the second pulse. Absorption within the existing ablation plume is observed and a channel of excited material is formed within the shock wave front. This excitation causes a second shock wave with a center above the material surface which has a faster expansion velocity at this time than the shock wave caused by the first pulse. The existing shock wave is deformed due to the expanding elliptic shock wave after unification. The elliptic shock wave has a non-negligible downward directed part which could direct particles towards the sample surface again. In combination with the decreased ablation efficiency for 2 PpB, this result supports the thesis of redeposition of the material for this pulse configuration. A pronounced melt dynamic within the ablation crater is assumed due to the dense surface bulge and the SEM images. A particle-based ablation plume is observed as long-term behavior after the second pulse after disintegration of the bulge. In contrast, no channel formation is observed for 3 PpB after the third pulse. After the absorption of the pulse, which is also observed within the existing ablation plume, a fast propagating semitransparent hemisphere is observed. The semitransparent ablation products spread primarily laterally and are interpret as vapor phase. In addition to the vapor-based ablation share, a particle-based ablation plume is still present in the long-term behavior. This is interpreted as one reason for the efficiency increase observed for 3 PpB and is supported by the observed melt structure within the ablation crater. Evident

reasons for the formation of a vapor-based ablation share are the preheating by intra-burst heat accumulation and the reduced atmospheric pressure due to the expanding shock wave. Additionally, the observed melt structure after the second pulse potentially benefits the absorption of the third pulse by a molten surface layer [16,34] which leads to a further increased ablation depth for 3 PpB. Similar to 3 PpB, for 4 PpB no channel formation but a vapor-based ablation share is observable. However, the vapor share is less pronounced compared to 3 PpB. For all bursts a particle-based ablation is observed after the last pulse of the burst. For further investigations and a deeper insight of the USP burst ablation of metals, an in situ comparison of different ablation regimes is necessary. Furthermore, a detailed analysis of the long-term ablation dynamics should be performed. Additionally, an investigation of different materials and multi burst ablation is reasonable.

Acknowledgments and Appendixes

This research was supported by the German Federal Ministry of Education and Research (BMBF).
(Forschungscampus Digital Photonic Production 13N15423)

References

[1] S. Nolte, C. Momma, H. Jacobs, A. Tünnermann, B. N. Chichkov, B. Wellegehausen, and H. Welling: J. Opt. Soc. Am. B, 14, (1997) 2716.

[2] B. N. Chichkov, C. Momma, S. Nolte, F. Alvensleben, and A. Tünnermann: Appl. Phys. A, 63, (1996) 109.

[3] C. Momma, B. N. Chichkov, S. Nolte, F. von Alvensleben, A. Tünnermann, H. Welling, and B. Wellegehausen: Opt. Commun., 129, (1996) 134.

[4] J. Schille, L. Schneider, A. Streek, S. Kloetzer, and U. Loeschner: Opt. Eng, 55, (2016) 96109.

[5] J. Finger and M. Reininghaus: Opt. express, 22, (2014) 18790.

[6] T. Kramer, B. Neuenschwander, B. Jäggi, S. Remund, U. Hunziker, and J. Zürcher: Phys. Procedia, 83, (2016) 123.

[7] A. Ancona, S. Döring, C. Jauregui, F. Röser, J. Limpert, S. Nolte, and A. Tünnermann: Opt. Lett., 34, (2009) 3304.

[8] A. Ancona, F. Röser, K. Rademaker, J. Limpert, S. Nolte, and A. Tünnermann: Opt. express, 16, (2008) 8958.

[9] G. Raciukaitis: J. Laser Micro/Nanoengin., 4, (2009) 186.

[10] S. Kraft, J. Schille, S. Mauersberger, L. Schneider, and U. Loeschner, Proc. SPIE, Vol. 11268, (2020 - 2020) 54.

[11] A. Gillner, J. Finger, P. Gretzki, M. Niessen, T. Barthels, and M. Reininghaus: J. Laser Micro/Nanoengin., 14, (2019) 129.

[12] B. Neuenschwander, B. Jaeggi, M. Zimmermannn, V. Markovic, B. Resan, K. Weingarten, R. de Loor, and L. Penning: J. Laser Appl., 28, (2016) 22506.

[13] B. Neuenschwander, G. F. Bucher, C. Nussbaum, B. Joss, M. Muralt, U. W. Hunziker, and P. Schuetz, Proc. SPIE, Vol. 7584, (2010) 75840R.

[14] B. Jaeggi, B. Neuenschwander, M. Zimmermann, L. Penning, R. deLoor, K. Weingarten, and A. Oehler, Proc. SPIE, Vol. 8967, (2014) 89670Q.

[15] B. Jäggi, L. Cangueiro, D. Bruneel, J. A. Ramos de Campos, C. Hairaye, and B. Neuenschwander, Proc. SPIE, Vol. 10519, (2018) 4.

[16] B. Neuenschwander, T. Kramer, B. Lauer, and B. Jaeggi, Proc. SPIE, Vol. 9350, (2015) 93500U.

[17] N. Hodgson, H. Allegre, A. Starodoumov, and S. Bettencourt: J. Laser Micro/Nanoengin., 15, (2020) 236.

[18] B. Bornschlegel and J. Finger: J. Laser Micro/Nanoengin., 14, (2019) 88.

[19] J. Finger, B. Bornschlegel, M. Reininghaus, A. Dohrn, M. Nießen, A. Gillner, and R. Poprawe: Adv. Opt. Technol., 7, (2018) 145.

[20] J. Finger and M. Hesker: J. Phys. Photonics, 3, (2021) 21004.

[21] A. Gillner, P. Gretzki, and L. Büsing, Proc. SPIE, Vol. 9740, (2016) 974010.

[22] T. Barthels and M. Reininghaus, Proc. SPIE, Vol. 10744, (2018 - 2018) 10.

[23] B. Bornschlegel, J. Köller, and J. Finger: J. Laser Micro/Nanoengin., 15, (2020) 56.

[24] T. Kramer, S. Remund, B. Jäggi, M. Schmid, and B. Neuenschwander: Adv. Opt. Technol., 7, (2018) 129.

[25] F. Bauer, A. Michalowski, T. Kiedrowski, and S. Nolte: Opt. express, 23, (2015) 1035.

[26] A. Sassmannshausen, A. Brenner, and J. Finger: J Mater. Process. Technol., 293, (2021) 117058.

[27] D. J. Förster, S. Faas, S. Gröninger, F. Bauer, A. Michalowski, R. Weber, and T. Graf: Appl. Surf. Sci., 440, (2018) 926.

[28] T. Kramer: J. Laser Micro/Nanoengin., 12, (2017) 107.

[29] A. Žemaitis, P. Gečys, M. Barkauskas, G. Račiukaitis, and M. Gedvilas: Sci. reports, 9, (2019) 12280.

[30] B. Jäggi, D. J. Förster, R. Weber, and B. Neuenschwander: Adv. Opt. Technol., 7, (2018) 175.

[31] C. Wu and L. V. Zhigilei: Appl. Phys. A, 114, (2014) 11.

[32] M. Spellauge, J. Winter, S. Rapp, C. McDonnell, F. Sotier, M. Schmidt, and H. P. Huber: Appl. Surf. Sci., 545, (2021) 148930.

[33] J. Winter, S. Rapp, M. Spellauge, C. Eulenkamp, M. Schmidt, and H. P. Huber: Appl. Surf. Sci., 511, (2020) 145514.

[34] M. Brückner, J. H. Schäfer, and J. Uhlenbusch: J. Appl. Phys., 66, (1989) 1326.

(Received: October 15, 2021, Accepted: May 28, 2022)